Materials and Design 165 (2019) 107581

Contents lists available at ScienceDirect

Materials and Design

journal homepage: www.elsevier.com/locate/matdes

Improving plasticity of metallic glass by electropulsing-assisted surface severe plastic deformation

Chi Ma [a], Sergey Suslov [b], Chang Ye [a,*], Yalin Dong [a,*]

[a] Department of Mechanical Engineering, University of Akron, Akron, OH 44325, United States
[b] Qatar Environment and Energy Research Institute (QEERI), Qatar Foundation, Doha, Qatar

HIGHLIGHTS

- Electropulsing-assisted surface severe plastic deformation (EP-SSPD) treatment increased plasticity from 0% to 2.03% ± 0.29%.
- EP-SSPD generated a hybrid structure of 4.1% uniformly-distributed nanocrystals and 0.009% averaged extra free volume.
- Free volume alleviates localized strain at nanocrystal/matrix interface and nanocrystals retard shear band propagation.

GRAPHICAL ABSTRACT

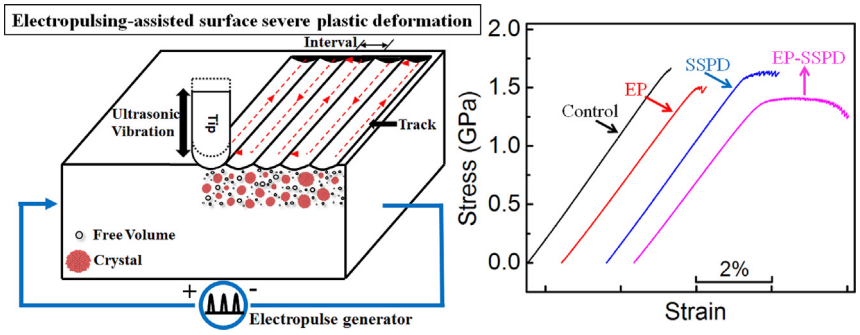

ARTICLE INFO

Article history:
Received 20 August 2018
Received in revised form 1 January 2019
Accepted 2 January 2019
Available online 4 January 2019

Keywords:
Structure heterogeneity
Electropulsing-assisted surface severe plastic deformation
Nanocrystals
Free volume
Metallic glass
Plasticity

ABSTRACT

Using either electropulsing (EP) or surface severe plastic deformation (SSPD) to process metallic glasses can improve their plasticity, however, the moderate improvement in plasticity does not warrant a commercial usage. This work, for the first time, demonstrates the integration of electropulsing and surface severe plastic deformation is much more effective in improving the plasticity of metallic glasses than EP or SSPD treatment alone, opening a new avenue towards an unprecedented combination of strength and plasticity in metallic glasses. It is found that SSPD can generate microstructure heterogeneity featured by a mixture of matrix and plastically displaced regions with increased atomic volume. When applying EP and SSPD simultaneously, a synergistic effect occurs to produce a hybrid network with excess free volume and nanocrystals uniformly embedded in amorphous matrix. Molecular dynamics simulation and fracture surface analysis further reveal that the hybrid network is able to effectively reduce shear band localization, and therefore delay the fracture of metallic glasses.

1. Introduction

The history of bulk metallic glasses (BMGs) can be traced back to the 1960s, when Duwez and his co-workers fabricated the first melt-quenched metallic glass in their laboratory [1]. Since then, metallic glasses have received significant scientific attention for their unique properties as compared with their crystalline counterparts. Due to their disordered atomic structure, metallic glasses possess many superior mechanical properties including high hardness [2], large elastic strain range [3], high wear resistance [4] and corrosion resistance [5]. As a double-edged sword, however, the amorphous structure of BMGs also leads to extremely low ductility for the lack of work-hardening during plastic deformation. During plastic deformation of BMGs, shear bands are nucleated to accommodate plastic strain. Because there are no dislocation-like barriers, the shear bands can readily be localized,

* Corresponding authors.
E-mail addresses: cye@uakron.edu (C. Ye), ydong@uakron.edu (Y. Dong).

https://doi.org/10.1016/j.matdes.2019.107581

and this often leads to a catastrophic failure of BMGs. The durability issue becomes a roadblock for the widespread use of BMGs. The first well-known commercialization trial was pioneered in the early 1990s by Johnson's team and the partner company, Liquidmetal Technologies, Inc., to use BMGs in the production of golf clubs [6]. Despite the BMG golf club gave rise to superior performance and was highly rated by golf players, the product failed to earn commercial success for its durability issue.

The efforts to seek methods to improve the ductility of BMGs have not ceased since their invention. Because fracture tends to initiate from the surface of a material, surface engineering is viewed as a promising technology in combating the fracture of BMGs [7–17]. Especially in recent years, surface severe plastic deformation (SSPD) techniques such as shot peening [18], laser shock peening [19–21], and surface mechanical attrition treatment [22] have been applied to treat BMG surfaces, and improvements in plasticity have been observed after SSPD treatment. These SSPD techniques modify the treated surface in two beneficial ways. First, compressive residual stress is produced to slow down the propagation of shear bands [18]. Second, microstructural heterogeneity featured by a mixture of matrix and severely plastically displaced region induced by SSPD also plays a significant role in delaying fracture [15,22,23]. Ultrasonic nanocrystal surface modification (UNSM) is a recently developed SSPD method that utilizes simultaneous ultrasonic striking to induce microstructure change and compressive residual stresses on a metal surface. Compared with traditional SSPD techniques, UNSM is more controllable and can achieve higher quality of surface finishing [24–30]. We should point out that while UNSM was firstly coined in the context of crystalline metals [27,31], the concept of grain refinement to nanoscale is inapplicable to metallic glass. In one of our previous works [32], we have demonstrated that UNSM can improve the fracture strain of BMGs. Through molecular dynamics simulation, we further reveal that shock wave resulted from SSPD can induce pre-displaced atoms (whose position is deviated from initial configuration) with an increased atomic volume [33], which can promote and delocalize shear bands.

In parallel with the exploration of SSPD treatment, attempts to use electropulsing (EP) to treat BMGs were also made [34–41]. The most striking effect of EP treatment is the generation of crystalline phases in BMGs [34–38]. The second phase if introduced during solidification could significantly improve the ductility of BMGs [42–50]. However, this is not the case for EP-treated BMGs [34–41]. The ductility was either moderately improved or became worse [41,51]. One possible reason is that EP treatment also causes structure relaxation [37,39–41] and thus reduces free volume, which is detrimental to ductility. It is thus not surprising that EP treatment garnered little attention from the BMG industry because of the disappointing gains in ductility. However, it inspires this work to combine EP with SSPD to fully use its advantages while suppressing its shortcomings.

In this work, we will demonstrate that the plasticity of BMGs can be remarkably improved by EP-assisted SSPD, much more effective than EP or SSPD treatment alone. To the best of our knowledge, this is the first time to combine EP and SSPD to treat BMGs, and more importantly the combined effect is remarkably significant, leading to an outstanding combination of strength and plasticity in BMGs. As a newly developed method, there is little knowledge about microstructure change induced by EP-SSPD. To fully use the potential of EP-SSPD, it is essential to establish the process–structure-performance relationships. A collaborative effort through experimental characterizations and molecular dynamics (MD) simulation is made to have a fundamental understanding of EP-assisted SSPD treatment of BMGs. The unique microstructure produced by EP-SSPD is revealed by experimental characterizations. The effect of microstructure on improving the plasticity of metallic glasses is elucidated through MD simulation as well as the analysis of fracture surface morphology. The research will advance our fundamental understandings of EP-SSPD on BMGs, enabling a low-cost and scalable surface engineering technology to increase the plasticity of BMGs. The fundamental understanding can be used to guide the design of BMGs with surface modification strategies and optimal process parameters.

2. Methodology

2.1. Materials

A Vit 1b BMG (44% Zr, 11% Ti, 10% Cu, 10% Ni, 25% Be, atomic percentage), belonging to the Vitreloy family fabricated by Materion, Inc., was used in this study. It was prepared through vacuum induction melting of commercially available purest elements under argon atmosphere. The as-received material had the dimensions of 121 by 100 by 5 mm in length, width and thickness respectively. The samples were cut into rectangular shape with the volume of 5 by 2.5 by 2.5 mm^3 using electric discharge machining.

2.2. Electropulsing-assisted UNSM

Ultrasonic nanocrystal surface modification (UNSM) was used to induce surface severe plastic deformation (SSPD). Therefore, the two terms, UNSM and SSPD, are interchangeable in this paper. As shown in the schematics in Fig. 1, the UNSM tip with a diameter of 2.4 mm generated 20 kHz ultrasonic vibration to strike the surface while at the same time, it scanned over the surface at 500 mm/min following the designed track with 10 μm interval. Static load 2 kg and dynamic load with 16 μm vibration amplitude (corresponding to free vibration) were simultaneously applied on the tip. Electropulse was applied to sample through an in-house electropulse generator. The characteristic pulse width was 100 μs, and the frequency can be adjusted from 100 Hz to 800 Hz. The maximum current density was controlled at ~70 A/mm^2. For 150 Hz and 450 Hz electropulsing treatments, the surface temperature was measured as 338 K and 473 K respectively by a K-type thermocouple (see Fig. S1 in Supplementary material). When UNSM was applied, because oil was applied to lubricate and cool the surface, no significant temperature rise was observed. One objective of the work is to differentiate the effect of electropulsing-assisted UNSM (EP-UNSM) from that of EP and UNSM alone. Therefore, four groups of samples were prepared including untreated (control) samples, UNSM-treated samples, EP-treated samples and EP-UNSM samples.

2.3. Microscope observation

The generated nanocrystals after treatment were characterized by transmission electron microscope (TEM), and the fracture surfaces after compression test were observed by scanning electron microscope (SEM). TEM samples were prepared using the focused ion beam (FIB) lift-out method. For 450 Hz EP-treated sample, the TEM sample was fabricated by FEI Helios Nanolab 650 with Ga ion beam and observed in FEI Tecnai F30 with 300 kV operating voltage. For 450 Hz EP-UNSM sample, the sample was prepared by FEI Versa 3D LoVac FIB-SEM system and characterized in FEI Talos F200X which is a scanning transmission electron microscope (STEM) at 200 kV. For each treatment, one sample was prepared for the TEM characterization. The fracture surfaces of all samples were observed using an FEI Quanta 200 scanning electron microscope operated at 30 kV.

2.4. Differential scanning calorimetry (DSC)

Thermal stability and free volume were measured by differential scanning calorimetry (DSC) tests [52–54]. The scanning temperature increased from room temperature to 810 K which is above crystallization temperature (739 K). The heating rate was 0.33 K/s and cooling rate was 1.66 K/s. Two scans were conducted and their difference was the sample's heat flow during the process of structural relaxation and crystallization. A thin layer was first cut and then gradually polished using

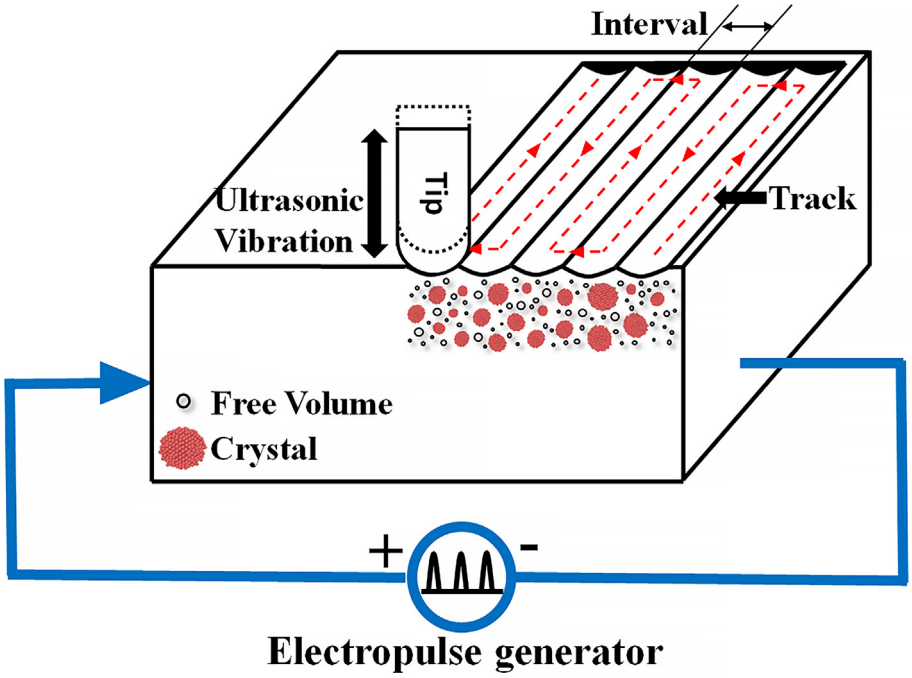

Fig. 1. Schematics of electropulsing-assisted UNSM process.

600 grid sandpapers. The final dimensions of measured sample were controlled around 3.5 by 2.4 by 0.3 mm.

2.5. In-depth hardness

All samples were first cut and mounted in epoxy. To acquire clear indentations, polishing via SiC paper and 3 μm colloidal silica suspension was conducted on the cross-sections. A hardness tester, Wilson Tukon 1202, was used to measure in-depth hardness ranging from 0 to ~120 μm. 100 g load and 10 s indent duration were applied.

2.6. Compression test

An Instron 5582 universal testing machine was used to carry out compression test at room temperature. A loading rate of 0.025 mm/min (corresponding to a strain rate of 8.33×10^{-5}/s) was used to carry out all compression tests. The applied external load was recorded to calculate engineering stress and the displacement was used to calculate engineering strain.

2.7. Molecular dynamics simulation

In one of our previous studies [33], we have employed MD simulation to reveal that SSPD can induce pre-displaced atoms with an increased atomic volume, which promotes and delocalizes shear bands. In this work, MD simulation was conducted to elucidate how the hybrid microstructure (composite microstructure with nanocrystals, extra free volume, and amorphous matrix) induced by EP-SSPD affects shear band formation and propagation during the plastic deformation of metallic glass. A binary metallic glass composite $Zr_{71}Cu_{29}$ containing Zr_2Cu nanocrystals was constructed to mimic the EP-SSPD treated BMG Vit 1b. The interatomic potential of zirconium (Zr) and copper (Cu) atoms was simulated by an embedded atom method (EAM) potential [55]. The system was firstly equilibrated at 2200 K with NPT ensemble ($P = 0$ bar) at a time step of 1 fs to reach the amorphous liquid state. A fast cooling process at a rate of 1 K/ps was applied to reduce the temperature to 300 K. For metallic glass matrix composites, spherical Zr_2Cu nanocrystals (3 nm in diameter) were randomly inserted by deleting overlapped amorphous matrix atoms. After equilibrium at 300 K, the final metallic glass matrix composite with dimension of 12 (x) by 12 (y) by 30 (z) nm was prepared. Tension tests were conducted at a strain rate of 1×10^8/s with NVT ensemble ($T = 300$ K). Free boundary conditions were applied on all surfaces. Large-scale atomic/molecular massively parallel simulator (LAMMPS) was used to conduct molecular dynamics simulation [56] and the Open Visualization Tool (Ovito) was adopted for post visualization process [57].

3. Results

3.1. Brittle to ductile transition

We first conducted compression tests of samples with three types of treatment, namely, EP, UNSM, and EP-UNSM, along with control sample without any treatment. Fig. 2 shows the compressive stress-strain curves measured by the Instron 5582 universal testing machine at room temperature. An initial non-linear region is observed for all

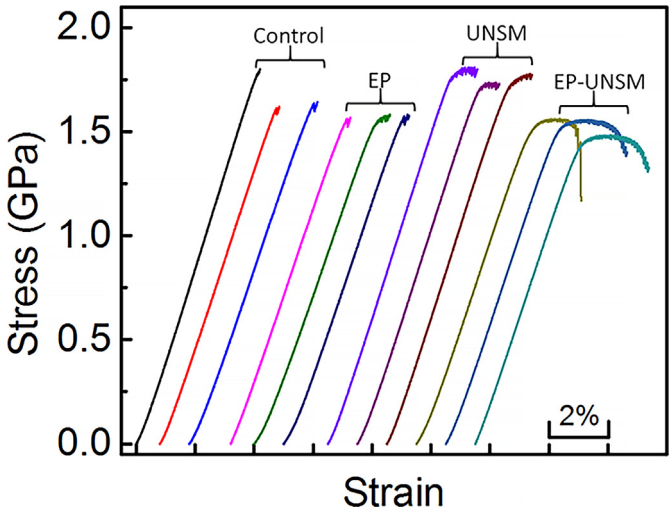

Fig. 2. Compressive stress-strain curves of control, 450 Hz EP, UNSM, and 450 Hz EP-UNSM samples (each with three repetitions).

samples [18,58,59], which is caused by the process of getting solid contact between sample and loading plate (see Fig. S2 in Supplementary material for one representative stress-strain curve of UNSM-treated sample). The control samples only show elastic regime and fracture at a stress of 1.69 ± 0.10 GPa, manifesting the brittle nature of the studied material. For the EP-treated samples, a marginal increase of plastic strain (the strain after 0.2% offset yield point) of 0.16% ± 0.18% is observed while the ultimate fracture stress is decreased to 1.58 ± 0.006 GPa. The EP treatment alone does not give rise to a significant improvement in plasticity, which is consistent with the literature [41]. After UNSM treatment, the samples do exhibit a plastic strain of 0.63% ± 0.15%. More importantly, the material strength (maximum stress before fracture) increases to 1.77 ± 0.04 GPa. In our previous works [32,33], we have elucidated that UNSM can induce pre-displaced atoms with an increased atomic volume, which promote and delocalize shear bands. Therefore, instead of catastrophic fracture observed in the control samples with localized shear bands, UNSM samples contain more shear bands and their propagation is suppressed due to the interaction of shear bands, which leads to increased material strength [32]. When combining EP and UNSM together, the material strength decreases to 1.53 ± 0.05 GPa and the improvement of plastic strain becomes significant, 2.03% ± 0.29% compared with that for the control samples and EP-treated samples, and 0.63% ± 0.15% for the UNSM-treated samples. In addition to the improved plasticity, the fracture fashion of the EP-UNSM samples is also fundamentally altered, i.e., there is an alleviated stress drop before fracture, indicating the transition from a sudden brittle fracture to a plastic one. To the best of our knowledge, this is the first report to show the remarkable effect of EP-UNSM treatment on improving plasticity of BMGs. As a newly developed method, there is little understanding about how the hybrid EP-UNSM process alters the microstructure of BMGs, and how the microstructure change dictates mechanical properties. Towards that, in the following sections of the paper, we will establish the process–structure relationship through experimental characterization, and bridge structure modification and property enhancement through MD simulation and experimental investigation.

3.2. Process-structure relationship

3.2.1. Nanocrystals characterization

In this section, TEM measurement was carried out to reveal the microstructure change, especially crystallization, after EP-UNSM treatment. Metallic glasses without any treatment exhibit complete amorphous structure [9,60,61]. UNSM treatment and other surface severe plastic deformation techniques do not alter amorphous nature of metallic glasses, which has been approved in the literature [23,62] include including ours [32]. For EP treatment, it has been well recognized that EP induces crystallization in metallic glasses [34–38]. The fundamental question we want to examine here is what is the difference between EP induced crystallization and EP-UNSM induced one. To this end, TEM characterizations were carried out on the cross section near the treated surfaces of EP and EP-UNSM samples. The first row of Fig. 3 shows the characteristic of nanocrystals induced by EP at different magnifications, while the second row is from EP-UNSM sample. From the low magnification images (Fig. 3a and d), the striking difference is the spatial distribution of nanocrystals. The EP-induced nanocrystals tend to aggregate, and the closer to the surface the aggregation is more severe. In constrast, the nanocrystals induced by EP-UNSM are uniformly distributed in the subsurface. The size of nanocrystals can be obtained from high magnificantion images. Fig. 3b is a high magnification image at a dense region of Fig. 3a, and Fig. 3c is from the sparse region of Fig. 3a. It can be seen that the size of EP-induced nanocrystals is around tens of nanometer, for example, 41 nm for crystal "1" marked in Fig. 3b. For nanocrystals induced by EP-ENSM, however, their size varies significantly. In addition to the nanocrystals (32 nm for crystal "2" marked in Fig. 3e) comparable to EP-induced ones, it also contains many smaller nanocrystals (some of them are smaller than 10 nm, for example, "3" in Fig. 3e). The quantitative analysis is provided in Fig. 4. Firstly, a region of 3.48 by 3.48 μm^2 was selected from Fig. 3a and b respectively and then they were converted to grayscale images as shown in Fig. 4a and b. The area of each black region (one nanocrystal) was calculated and the radius was obtained by assuming spherical nanocrystals. For the EP sample, the nanocrystal fraction (the ratio of area of all the black regions to that of the whole region) is 3.9% while the nanocrystal fraction of EP-UNSM sample is 4.1%. For the EP sample, the nanocrystal radius ranges from 2.58 to 140.82 nm and there are 1.9% nanocrystals (number ratio) with radius over 80 nm. For the EP-UNSM sample, the size is from 2.51 to 64.50 nm. Fig. 4c shows the radius distribution from which it can be clearly seen that EP-UNSM generates more small-size nanocrystals. At present, TEM characterization was conducted near surface. Within the surface layer, both the spatial distribution and size spectrum of nanocrystals fabricated from EP-UNSM are different from those exhibited in EP samples. Compared with EP treatment, the microstructure produced by EP-UNSM contains more small-size nanocrystals, and more importantly, the distribution of nanycrystals are more uniform. While properties of crystalline phase

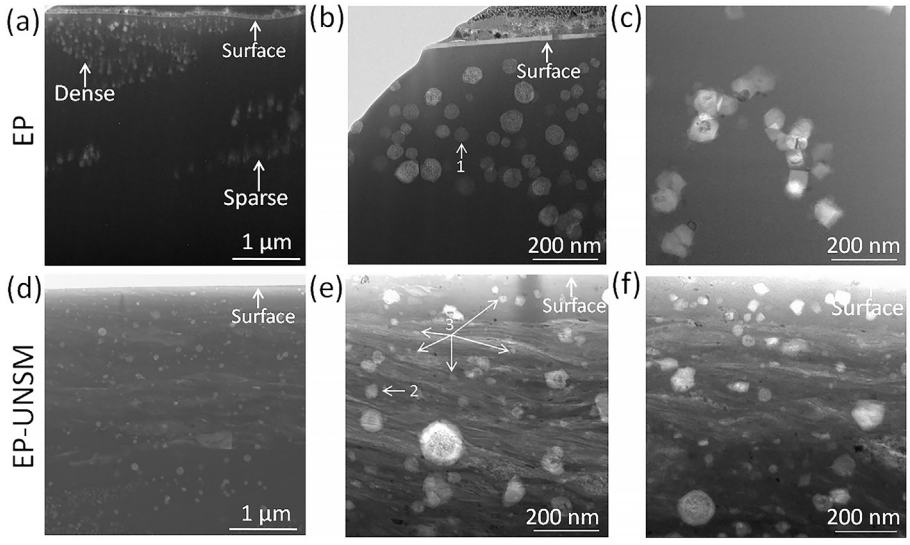

Fig. 3. Bright field TEM images of (a)–(c) the EP sample and STEM images of (d)–(f) the EP-UNSM sample at different magnifications. (b) is from the dense region where nanocrystals are aggregated in the EP sample. (c) is from the sparse region. (e) and (f) are two random regions near surface in the EP-UNSM sample.

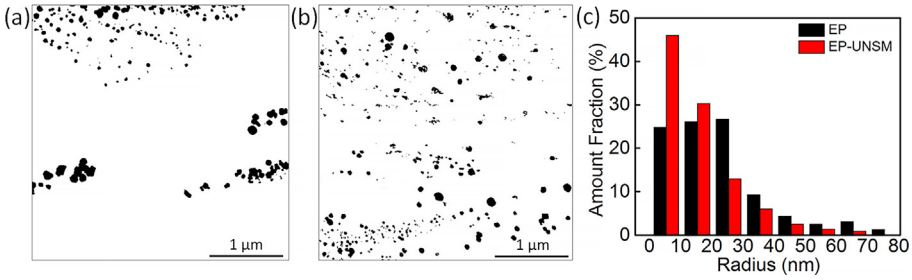

Fig. 4. Processed grayscale images of the 3.48 by 3.48 μm^2 region for the (a) EP sample and (b) EP-UNSM sample. (c) Distribution of nanocrystals' radius in EP and EP-UNSM sample when assuming spherical shape.

affect composite plasticity [63–65], nanocrystals with uniform dispersion are generally beneficial for plasticity improvement [66–68]. Relating to their plasticities as shown in Fig. 2, we argue that the difference in plasticity is resulted from the microstructure difference, which will be explored in Section 3.3.

Another interesting observation is that the structure of nanocrystals induced by EP-UNSM is also different from that shown in the EP sample. Fig. 5a and b exhibit the high resolution images of representitive crystals generated by EP and EP-UNSM respectively. The nanocrystals induced by EP show multiple close-packed directions (red dash lines) while the nanocrystal by EP-UNSM only presents one close-packed direction. This can also be seen from the fast fourier transform (FFT) diffraction patterns. The diffraction pattern of EP contains several pairs of bright spots while that of EP-UNSM only contains one pair. The multiple close-packed directions in EP indicate that the crystallite, even though in nano size, contains multiple nanocrystals with varied orientations, and the single colse-packed direction in EP-UNSM indicates that it is a single crystal. Because the structures presented in Fig. 5 are representative for both EP and EP-UNSM, the structure difference suggests that there might be a fundamental difference in the nature of nucleation sites for EP and EP-UNSM. An intensive high-resolution TEM characterization and atomistic analysis are invited to reveal the exact mechanism of crystallization under EP and EP-UNSM treatment.

3.2.2. Free volume characterization

In metallic glass, free volume is referred as defects in terms of atomic stress [69]. It has been demonstrated that free volume induced by UNSM is another key factor in determining the plasticity of metallic glasses [32,33]. This enlightens us to characterize free volume in the samples treated by different methods.

Direct observation of free volume and its dynamics is extremely challenging for its atomic characteristics. Experimentally, differential scanning calorimetry (DSC) is a routine technique to macroscopically measure free volume in metallic glasses [52–54,70,71]. The measurement is based on the well-established relation that enthalpy of relaxation is linear to free volume change, $\Delta H = \beta \Delta v_f$, where Δv_f is the free volume change per atomic volume [52,53,72]. For $Zr_{44}Ti_{11}Ni_{10}Cu_{10}Be_{25}$ metallic glass which is the same material used in this work, β has been measured as 623 kJ/mol [72]. The procedure to determine the enthalpy of relaxation during the release of free volume has been documented in [52]. In their work, the temperature was raised over crystallization temperature and two scans were conducted to obtain sample's heat flow (the difference of two scans [9]). Using the control sample as reference, the enthalpy of relaxation caused by extra released free volume induced by treatment can be determined by

$$\Delta H_i = \int_{T_1}^{T_2} \frac{w_i^{exp}(T) - w_i^{base}(T)}{c} - \int_{T_1}^{T_2} \frac{w_0^{exp}(T) - w_0^{base}(T)}{c} \quad (1)$$

where subscript *0* indicates control sample, *i* indicates samples with different treatments, w^{exp} represents sample heat flow, w^{base} is baseline heat flow and c is heating rate.

Fig. 6 shows the heat flow of different samples measured by DSC. For the control sample, glass transition (flow step) occurs at 638.3 K and crystallization temperature (flow peak) is 768.5 K. It has been reported the application of EP can reduce the glass transition and crystallization temperature due to reduced nucleation energy [37,61]. After EP and EP-UNSM treatment in our case, however, the glass transition and crystallization temperatures are not significantly varied (a shift less than 1 K). One possible reason that we do not observe dramatic changes in glass transition and crystallization temperature is that the affected thickness by EP and EP-UNSM is much smaller than that of the entire sample. There is also little difference in crystallization enthalpy (reflected by peak areas), which may originate from the same reason. Fig. 7 shows the corrected heat flow that can be used to calculate different enthalpy of relaxation according to Eq. (1). Below the heating

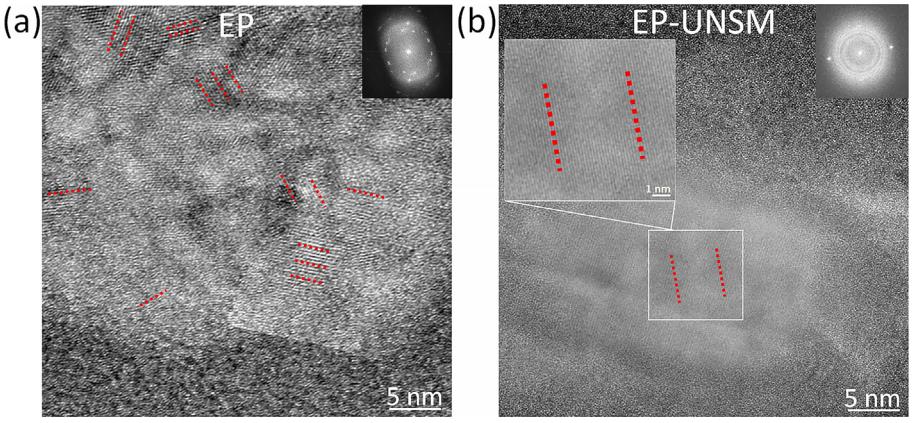

Fig. 5. High resolution images of nanocrystals in (a) EP and (b) EP-UNSM samples. Red dash lines represent the close-packed direction for the nanocrystals. For the EP sample, not all close-packed directions are marked. (For interpretation of the references to color in this figure legend, the reader is referred to the web version of this article.)

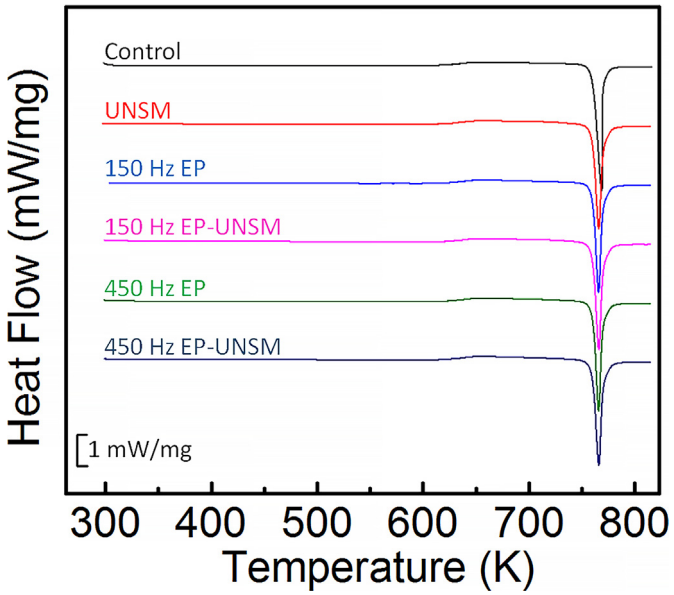

Fig. 6. Heat flow of samples with different treatments. The curves are shifted for visualization.

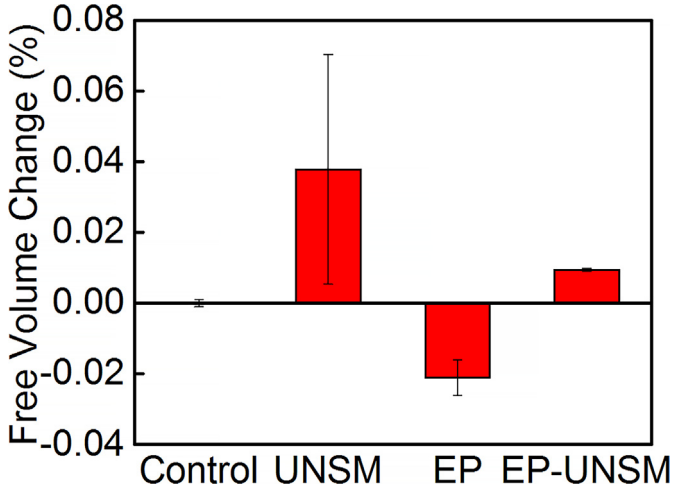

Fig. 8. Free volume changes of UNSM-treated samples, 450 Hz EP-treated samples and 450 Hz EP-UNSM samples, compared to the control samples. For each group, three samples were measured to calculate the error bars. The averaged free volume of the control samples is set as baseline.

temperature of 623 K, the trapped free volume is released due to increased atomic mobility. Therefore, the area surrounded by the heat flow curve and the zero line is the enthalpy of relaxation, which is used to calculate released free volume according to the linear relationship between enthalpy of relaxation and free volume change. Fig. 8 shows the free volume changes with error bars for the UNSM-treated sample, EP-treated sample, and EP-UNSM sample. UNSM induces an increase of 0.038% ± 0.032% free volume, which is consistent with other SSPD works, for example, 0.037% after laser shock peening [54]. EP-UNSM also generates extra free volume of 0.009% ± 0.0003%. In contrast, EP treatment reduces free volume by 0.021% ± 0.005%. Based on TEM and DSC analysis, we can see, although nanocrystalline phase is generated by EP (see Fig. 3a), which is beneficial to plasticity improvement, the reduction of free volume is detrimental to plasticity. The competition between the two mechanisms leads to an insignificant gain in plasticity. When combining EP and UNSM treatment, on the one hand it induces free volume compared with control sample but less than that of UNSM-treated sample; on the other hand it induces nanocrystalline phase. The hybrid network of both nanocrystalline phase and free volume has a synergistic effect on improving plasticity.

3.2.3. In-depth hardness

Hardness is a measure of the resistance of a material to plastic deformation, and thus can be used as an indicator of materials microstructure. Fig. 9a exhibits the in-depth hardness of EP-treated samples with 150 Hz and 450 Hz pulse currents. While the hardness of Vit 1b measured previously is around 560 Hv [32], EP treatment decreases the surface hardness. This is attributed to the addition of nanocrystals, which induces interfaces between crystalline and amorphous phase. Interfaces can contribute to the initiation of shear bands during deformation [73,74] and therefore reduce the required force to generate plastic deformation, leading to material softening. The in-depth change of hardness further suggests there is a spatial distribution of produced nanocrystals, which gradually decreases along the depth. The spatial distribution can be explained by the "skin" effect of electric pulse current. When a pulse current passes through a conductor, the current varies on the cross section. The largest current density arises at the surface and decays into the material. As a result, its effect on the microstructure modification also decreases along the depth.

Fig. 9b shows the in-depth hardness of UNSM and EP-UNSM treated samples. As revealed in our previous works [32,33], UNSM-induced shock wave induces free volume in metallic glass and results in surface softening with surface layer hardness 525 Hv (average of the first three in-depth hardness data). The depth of softened metallic glass is 40 μm. We want to point out that the affected region can be deeper than the softened region. In our previous work, the depth of softened layer reaches 100 μm with a larger UNSM load while the depth of compressive residual stress goes to 200 μm [32]. Compared with UNSM-treated sample, the EP-UNSM treated samples also exhibit surface softening, but less severe (e.g. averaged hardness of 542 Hv for 450 Hz EP-UNSM sample). When compared with their EP-treated counterparts (e.g. 536 Hv for 450 Hz EP-treated sample), the surface softening of

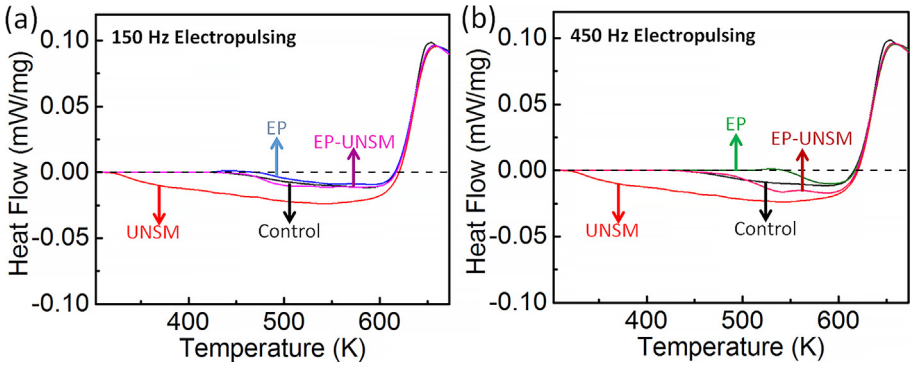

Fig. 7. Heat flows of (a) 150 Hz EP, EP-UNSM samples and (b) 450 Hz EP, EP-UNSM samples within the temperature range from 303 K to 673 K.

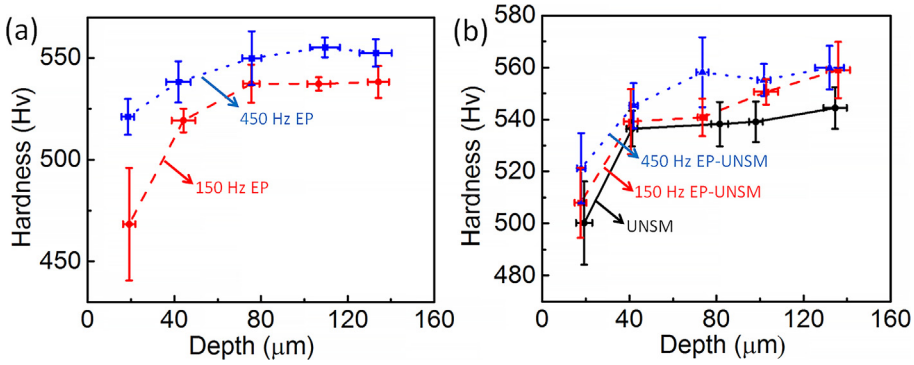

Fig. 9. Hardness distribution along depth (a) for 150 Hz EP and 450 Hz EP samples and (b) for UNSM, 150 Hz EP-UNSM and 450 Hz EP-UNSM samples.

the EP-UNSM treated samples is less severe too. Hardness is a measure of material's resistance to localized plastic deformation. In the context of metallic glass, plastic deformation occurs through the initiation and propagation of shear bands. Both excess free volume and nanocrystals can serve as nucleation sites for shear bands, and therefore lower hardness of metallic glass. According to Figs. 3a and 8, EP sample possesses larger and aggregated nanocrystals and UNSM sample contains more free volume. The nanocrystal aggregation in EP sample and excess free volume in UNSM sample lead to more severe material softening compared with EP-UNSM sample.

3.3. Structure-plasticity relationship

We have experimentally demonstrated that EP-UNSM produces a hybrid network of nanocrystals and free volume, which is assumed to be responsible for the enhanced plasticity of EP-UNSM treated metallic glass. This section is to establish the structure-plasticity relationship thorough molecular dynamics (MD) simulation and fracture surface analysis.

3.3.1. Molecular dynamics simulation

It is tremendously challenging to experimentally "see" the microstructure evolution of metallic glass during deformation. MD simulation thus becomes a powerful tool to provide dynamic information at atomic level for the fundamental understanding of microstructure-plasticity relationship.

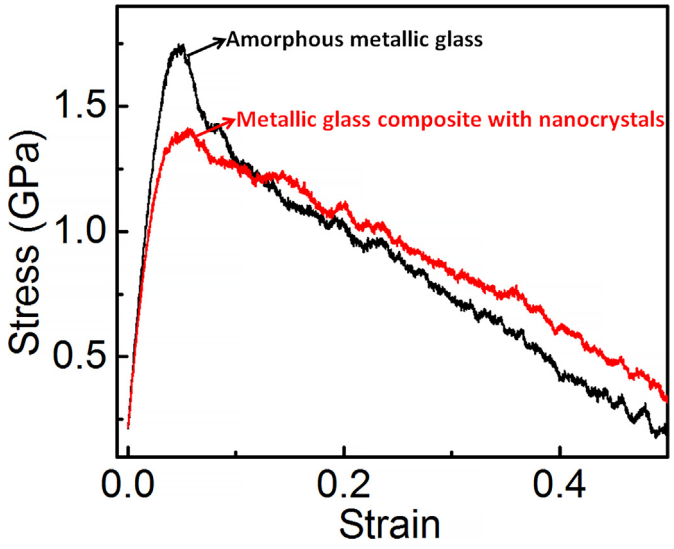

Fig. 10. Stress-strain curves of amorphous metallic glass and metallic glass composite with nanocrystals.

The effect of nanocrystals alone on the plasticity is investigated first. The stress-strain behavior of the glass composite (10% nanocrystals in volume), along with that of its amorphous counterpart, is presented in Fig. 10. The typical stress-strain curve contains a linear elastic deformation regime, and a plastic deformation regime. First we can see that the addition of nanocrystals reduces the yield stress from 1.74 GPa to 1.4 GPa at the strain of 0.05. However, the stress dropping rate is substantially delayed, indicating an improved plasticity. To unravel the effect of nanocrystals on the formation and propagation of shear bands, the atomic strain, a good indicator for shear bands [75–78], at different deformation stages (0.1 strain and 0.2 strain) is presented in Fig. 11. The amorphous metallic glass is also presented as comparison. Without nanocrystals, a localized shear band forms and grows rapidly in the middle region, leading to the necking and thus failure of the materials (Fig. 11a and b). In contrast, the presence of nanocrystals, on the one hand, assists the initiation of shear bands at the nanocrystal/matrix interface in the early stage; and on the other hand delays the growth of the shear bands into a major one, which is consistent with that reported in the literature [73,74]. As a result, the plasticity of the composite is improved.

To study how the nanocrystal/matrix interface promotes the initiation of shear bands, the atomic volume and von Mises strain [32,75] along the radial direction of nanocrystals are calculated. Considering the composite contains many nanocrystals, the averaged radial distribution is computed to reduce the statistical fluctuation. The calculation procedure is described as follows. The distance between each atom and its closest nanocrystal is first calculated as the radial coordinate. Based on the distance, atoms are divided into 50 segments, and the averaged atomic volume at initial configuration as well as von Mises strain at an overall strain of 0.07 are calculated. As shown in Fig. 12a, the atoms within nanocrystals possess smaller atomic volume (~19.9 $Å^3$) than that of atoms in amorphous state (~20.5 $Å^3$). In the interfacial region, the atomic volume experiences a sharp change. Fig. 12b shows the radial distribution of atomic von Mises shear strain at the overall strain of 0.07, which is used to characterize plastic deformation [75,76]. For the strain calculation, the reference configuration is the un-deformed state. Atomic strain gradually increases from the nanocrystal center to the interface, and then decreases slowly into the amorphous matrix. At the interface (~2.2 nm), the maximum strain arises. The inset in Fig. 12b shows a single nanocrystal and its nearby atomic strain field at the overall strain of 0.07. The two circles (dash lines) correspond to 1.5 nm and 2.2 nm radial distance respectively. It can be seen that there are ~4 atom layers between nanocrystal surface and maximum strain site. The higher mobility of atoms at the interface during the plastic deformation suggests that the nanocrystal/matrix interface promotes the initiation of shear bands.

After elucidating the effect of nanocrystals, we further study the synergistic effect of the hybrid network of nanocrystals and free volume. To prepare the system, free volume was first added in an amorphous matrix by randomly removing atom clusters (each cluster consists of four

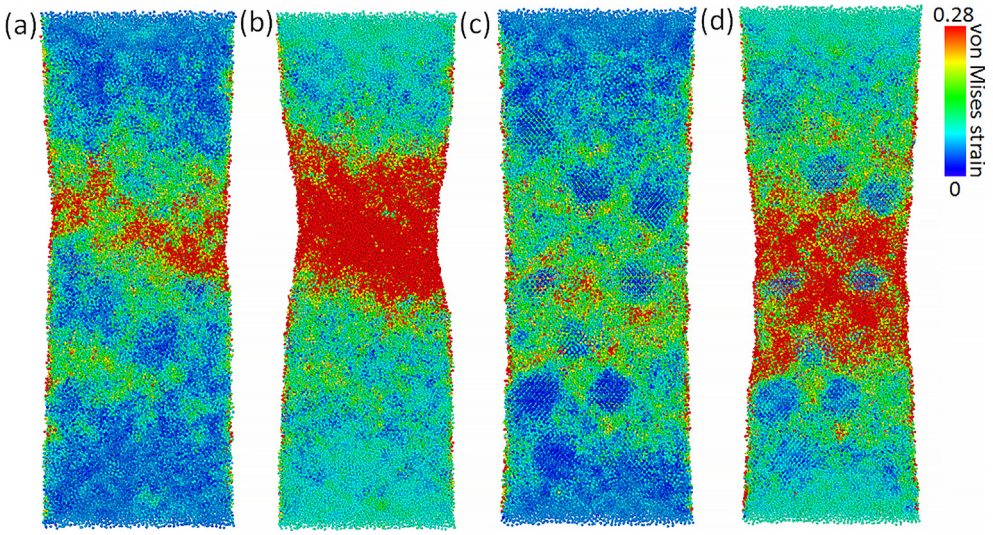

Fig. 11. Distributions of atomic von Mises strain for amorphous metallic glass at the strain of (a) 0.1 and (b) 0.2 and metallic glass matrix composites at the strain of (c) 0.1 and (d) 0.2.

atoms) [33]. Following the creation of free volume, Zr_2Cu nanocrystals (3 nm in diameter) were then inserted randomly. The systems were then equilibrated at 300 K over 1.6 ns with constant pressure (0 bar) and temperature (NPT ensemble) to reach thermodynamic equilibrium using system pressure and volume as indicators.

Fig. 13 presents the tensile behaviors of metallic glass composites with free volume only, nanocrystals only, and nanocrystals plus 2% (number ratio) and 4% free volume, respectively. One interesting observation is that the addition of free volume does not change the maximum stress notably, all are around 1.4 GPa. However, the stress drop rate (reflecting material degradation) is appreciably decreased with the increase of free volume. The specific stress drop rates (fitted slope of the region after maximum stress) are 2.2 GPa, 2.3 GPa, 2.1 GPa, and 2.0 GPa for composites with free volume only, with nanocrystals only, with nanocrystals plus 2% free volume, and with nanocrystals plus 4% free volume respectively. The decreased rates indicate improved plasticity with the hybrid microstructure. We further analyze the atomic strain distribution to gain insight into the mechanisms behind. The atomic strain distributions on the cross sections of composites with nanocrystals only and with nanocrystals plus 4% free volume at two strain stages are plotted in Fig. 14. In absence of free volume, as shown in Fig. 14a, most shear bands (red particles) tend to form near the nanocrystals at the early stage of plastic deformation (0.07 overall strain). For the composite with nanocrystals plus 4% free volume at the same overall strain of 0.07 (Fig. 14c), shear bands arise both in matrix due to the existence of free volume as well as near nanocrystals. With the continuous deformation to 0.2 overall strain, the composite with hybrid structure (Fig. 14d) contains more shear bands, and the distribution of shear bands is more uniform, compared with the composite with nanocrystals only (Fig. 14b). The incubation of more shear bands, in conjunction with a more uniform distribution, leads to the stronger interaction between shear bands, and thus delays their propagations. As a result, the hybrid free volume-crystallite structure gives rise to an improved plasticity, superior to stand-alone free volume or nanocrystal structure.

To further reveal the synergistic effect of the hybrid structure, the radial strain distribution for composites with nanocrystals only and nanocrystals plus 4% free volume is shown in Fig. 15. The atomic strain evolutions at different overall strains from 0.01 (initial elastic deformation) up to 0.07 (plastic deformation) are presented. With nanocrystals only, the nanocrystal/matrix interface sustains excess deformation (manifested by higher strain) compared with both matrix and nanocrystal (Fig. 15a). Considering that the interface is the mechanical weak point and the interface in reality may contain defects, not comparable to the ideally fused one in our simulation, the excess deformation at the interface can cause an early failure of the material. When there are nanocrystals and free volume simultaneously, the distribution of excess strain is changed and atoms at the interface have almost the same strain as that of atoms in the matrix as shown in Fig. 15b. This analysis provides molecular evidence for the synergistic effect between free volume and nanocrystals, i.e., the presence of free volume can alleviate the localized excess strain formed at the nanocrystal/matrix interface.

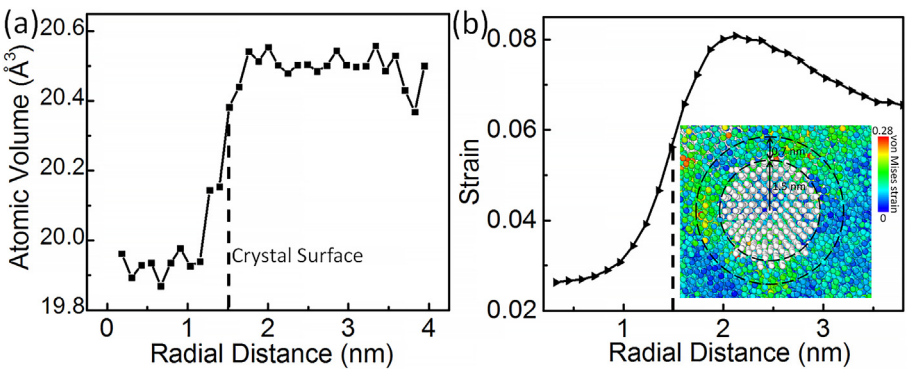

Fig. 12. Radial distribution of (a) atomic volume at initial configuration and (b) von Mises strain for metallic glass composite at the strain of 0.07. The insets exhibit the strain distribution of amorphous matrix around one nanocrystal and the strain of atoms inside the nanocrystal (white atoms) is not shown.

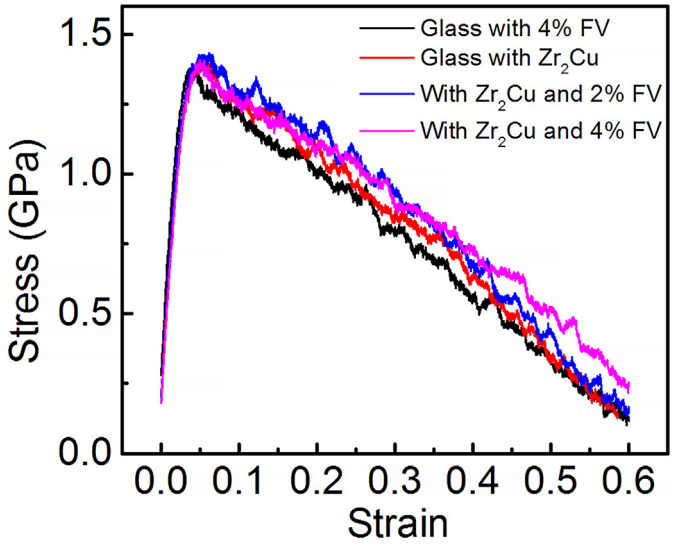

Fig. 13. Stress-strain curves of metallic glass containing free volume only, Zr_2Cu nanocrystals only, and nanocrystals with different fractions of free volume (FV).

3.3.2. Fracture mechanism

Fracture surfaces of samples subjected to different treatments were characterized, aiming to gain insights into how shear bands form and interact during fracture. Similar to the literature [79,80], it is observed that the fracture of metallic glass under compressive loading is shear dominated, which can be demonstrated by near 45° fracture angle (control 41°, EP 43°, UNSM 42°, EP-UNSM 49°). Fig. 16 exhibits the fracture surfaces of control, EP, UNSM, and EP-UNSM under different magnifications. The low magnification images (the first row) show the entire fracture surfaces. The control sample presents a relatively complete surface, indicating one crack source and a rapid fracture process. In contrast, the fracture surfaces of EP, UNSM, and EP-UNSM all consist of multi-surfaces. Particularly, crack steps, which are indicators for impeded crack propagation, are observed on the fracture surfaces of UNSM and EP-UNSM samples.

On the fracture surfaces at higher magnifications (the 2nd row and 3rd row in Fig. 16), typical arc-shaped patterns [79], are observed on the fracture surfaces of the control and EP-treated samples. The similar feature on their fracture surfaces is also consistent with their stress-strain behaviors, i.e., both samples with control and EP treatment present little plasticity. For the UNSM sample, in addition to the close-packed arc-shaped features, river-like patterns with clear primary and secondary structures also emerge on the fracture surface. For the EP-UNSM sample, the river-like patterns dominate, and moreover, its secondary features (branches at smaller scale) also become pronounced. It seems that there is a continuous transition from arc-shaped feature to river-like feature associated with the increase of plasticity. In addition, with a close look at the primary and secondary structures of the EP-UNSM fracture surface, they display self-similarity at different scales. The geometrical similarity implies a physical similarity behind. It has been well recognized that the fracture feature is related to the perturbation of shear band during crack development. Hence, based on the two observations above as well as fracture theory, it is conjectured that the hierarchical river-like structure is a continuous development of the arc-shaped structure, and the driving force for the continuous development originates from the perturbation of shear bands resulted from excess free volume and nanocrystals. To rationalize the conjecture, an in-depth analysis based on fracture theory is given below.

Fracture morphology can be used to manifest the fracture nature of materials. For metallic glass, it has been long recognized that a fluid-like shear band layer forms at the shear plane between two fracture parts during fracture [81,82]. The break-up of the shear band layer can be viewed as the advance of air (a lower viscosity fluid) into the shear band layer (a higher viscosity fluid). At the interface of the two fluids (crack tip as shown in Fig. 17a), the so-called Taylor instability occurs, which is reflected by the formation of corrugation feature. The progressive rupture of the viscous fluid will lead to the formation of a steady state form of corrugation as shown in Fig. 17b and c. A quantitative model has been developed by Argon [81] to predict the wavelength of the steady wave formed at crack tip, which is determined by the gradient of normal stress at the interface of two fluids, written as $\lambda = 2\pi\sqrt{\chi(d\sigma/dx)}$, where χ is surface tention, and $d\sigma/dx$ is the stress gradient in space. Similar fracture morphology has been observed in various metallic glass fracture experiments including our result (the inset figure in Fig. 17c). This mechanism has been verified with analogue experiments, in which grease is placed between plates of materials to mimic shear band layer in metallic glass. The separation of the two plates also leads to the formation of arc-shaped pattern [83], indicating a universal mechanism underlying the two distinct systems.

The question becomes how to interpret the river-like hierarchical fracture morphology of EP-UNSM treated metallic glass. More

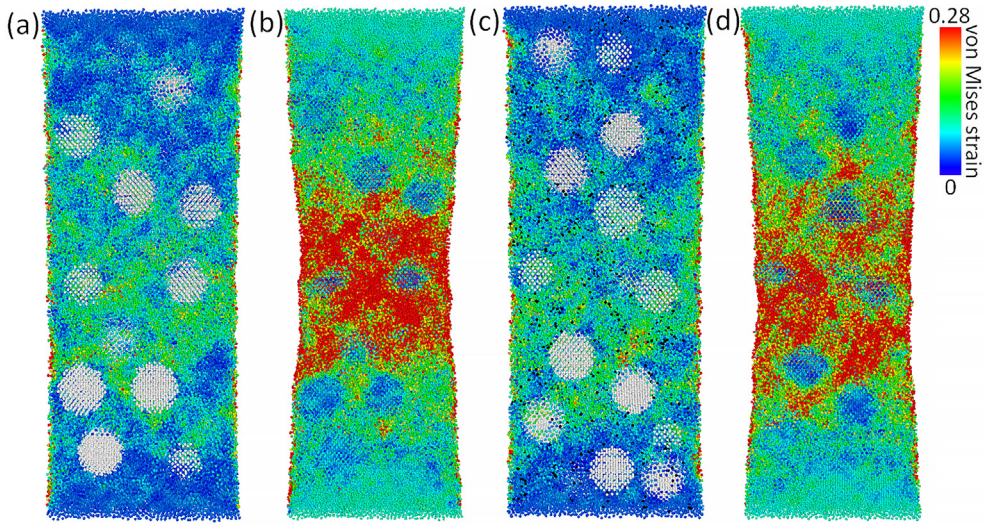

Fig. 14. Distributions of von Mises strain for metallic glass matrix composites with nanocrystals only at the strain of (a) 0.07 and (b) 0.2 and metallic glass matrix composites with nanocrystals plus 4% free volume at the strain of (c) 0.07 and (d) 0.2. The black particles in (c) are atoms initially nearby free volume. In (a) and (c), the strain of atoms in nanocrystals is not visualized to show the location of nanocrystals. (For interpretation of the references to color in this figure, the reader is referred to the web version of this article.)

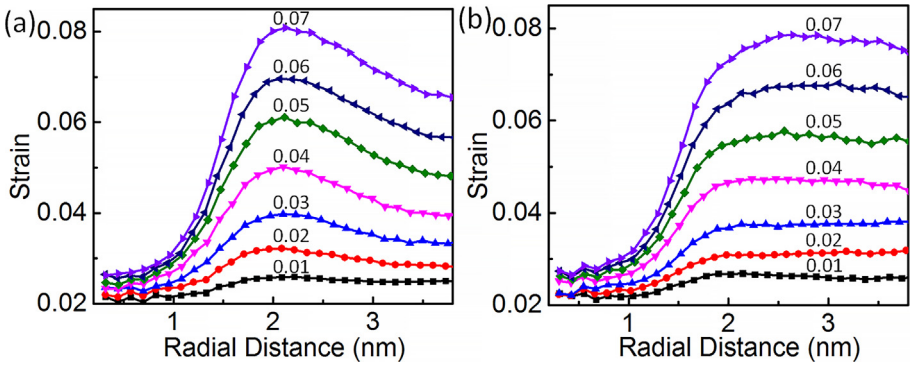

Fig. 15. Radial strain distribution at overall strains from 0.01 to 0.07 for (a) metallic glass matrix composites with nanocrystals only and (b) metallic glass matrix composites containing nanocrystals plus 4% free volume.

specifically, while we have identified that a hybrid network with both excess free volume and nanocrystalline phase is produced in EP-UNSM treated samples, what is the role of the microstructure in forming the river-like hierarchical pattern? As revealed by MD simulation, the existence of nanocrystals and free volume induces heterogeneity during the formation of shear band. Unlike the formation of a single localized shear band without nanocrystals and excess free volume (Fig. 11b), metallic glass with nanocrystals generates more shear bands uniformly embedded in matrix (Fig. 11d), forming a heterogeneous microstructure. The addition of excess free volume further increases the heterogeneity (Fig. 14d). When the crack tip advances, the heterogeneity can promote the formation of secondary corrugation superimposing on the primary corrugation as illustrated in Fig. 17d. The formation of secondary corrugation provides an additional energy dissipation channel for fracture. The additional energy dissipation channel through the secondary corrugation greatly increases the fracture toughness, and therefore delays the occurrence of fracture. The delay is reflected by the continuous growth of the primary corrugation. The growth will eventually lead to the coalescence of adjacent primary corrugations, forming the backbone of the river-like patterns. The secondary corrugation will grow into branches of the backbone. The formation of the hierarchical river-like pattern is schematically illustrated from Fig. 17d to g.

4. Conclusions

For the first time, we have demonstrated that EP-UNSM is much more effective in improving the plasticity of metallic glass than EP or UNSM alone, leading to a new avenue to achieve combined superior plasticity and strength in metallic glasses. UNSM treatment alone is able to generate heterogeneous microstructure with free volume uniformly embedded in amorphous matrix. EP treatment alone is able to generate nanocrystals at the expense of free volume annihilation, and

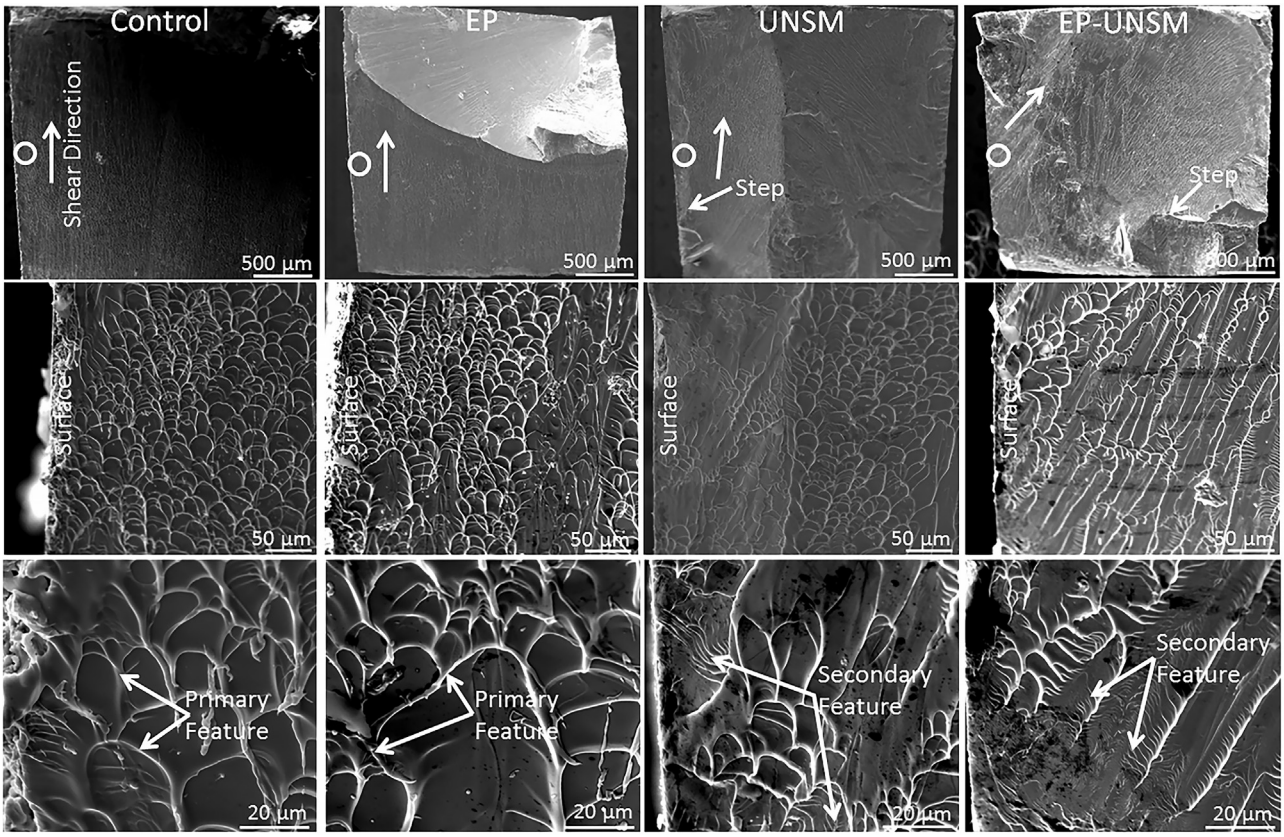

Fig. 16. Fracture surfaces of control, EP, UNSM and EP-UNSM samples after compression test.

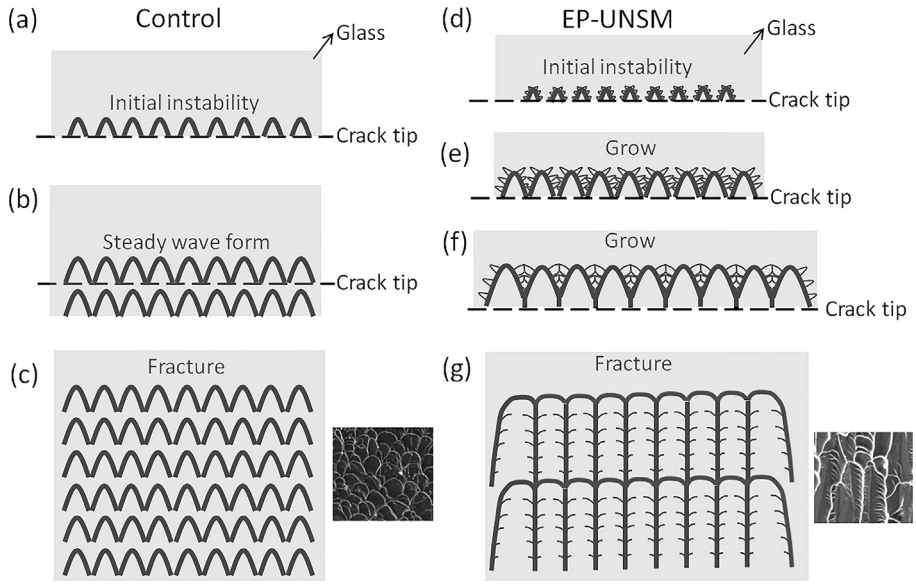

Fig. 17. Schematics of fracture process for control and EP-UNSM samples.

the nanocrystals tend to aggregate. The synergistic effect of EP-UNSM generates a hybrid structure with free volume and nanocrystals uniformly embedded in the amorphous matrix, leading to a significant improvement of plasticity from 0% to 2.03% ± 0.29%. As we have demonstrated in MD simulation, the presence of nanocrystals and free volume can both incubate shear bands and thus shear bands are uniformly distributed instead of the formation of one major shear band. The uniformly-distributed shear bands interact with each other, resulting in the delay of a catastrophic rupture typically observed in untreated metallic glasses. The work provides a novel, low-cost, and scalable surface engineering technique to produce BMGs with an outstanding combination of strength and plasticity. The fundamental understanding of how surface modification induced by EP-UNSM affects the microstructure and thus the plasticity of BMGs will provide a knowledge base to enable the design of an optimal processing strategy to fabricate BMGs with desirable properties.

Contributions made by authors

Chi Ma conducted most experiment and simulation work and wrote the first edition of draft.

Sergey Suslov helped to conduct TEM characterization.

Chang Ye and Yalin Dong supervised the entire work, applied funding to support the work, helped to analyze the results, and provided insightful discussion.

Acknowledgements

This work was supported by the startup funding from the College of Engineering and the Faculty Research Grant (#207335) at the University of Akron and the NSF CAREER program (CMMI 1847247). The authors are grateful for the help from Danqi Wang to carry out TEM charaterization. We would also like to thank the Imaging and Characterization CORE Labs at Qatar Environment and Energy Research Institute for the access to the FIB and TEM facilities.

Appendix A. Supplementary data

Supplementary data to this article can be found online at https://doi.org/10.1016/j.matdes.2019.107581.

References

[1] W. Klement, R.H. Willens, P. Duwez, Non-crystalline structure in solidified gold–silicon alloys, Nature 187 (1960) 869–870, https://doi.org/10.1038/187869b0.
[2] Z.Q. Liu, Z.F. Zhang, Strengthening and toughening metallic glasses: the elastic perspectives and opportunities, J. Appl. Phys. 115 (2014), 163505. https://doi.org/10.1063/1.4872249.
[3] W.L. Johnson, Bulk glass-forming metallic alloys: science and technology, MRS Bull. 24 (1999) 42–56, https://doi.org/10.1557/S0883769400053252.
[4] M. Ma, R. Liu, Y. Xiao, D. Lou, L. Liu, Q. Wang, W. Wang, Wear resistance of Zr-based bulk metallic glass applied in bearing rollers, Mater. Sci. Eng. A 386 (2004) 326–330, https://doi.org/10.1016/j.msea.2004.07.054.
[5] A. Inoue, Stabilization of metallic supercooled liquid and bulk amorphous alloys, Acta Mater. 48 (2000) 279–306, https://doi.org/10.1016/S1359-6454(99)00300-6.
[6] J. Plummer, W.L. Johnson, Is metallic glass poised to come of age? Nat. Mater. 14 (2015) 553–555, https://doi.org/10.1038/nmat4297.
[7] J.P. Chu, J.E. Greene, J.S.C. Jang, J.C. Huang, Y.L. Shen, P.K. Liaw, Y. Yokoyama, A. Inoue, T.G. Nieh, Bendable bulk metallic glass: effects of a thin, adhesive, strong, and ductile coating, Acta Mater. 60 (2012) 3226–3238, https://doi.org/10.1016/j.actamat.2012.02.037.
[8] C.C. Yu, J.P. Chu, C.M. Lee, W. Diyatmika, M.H. Chang, J.Y. Jeng, Y. Yokoyama, Bending property enhancements of Zr55Cu30Al10Ni5 bulk metallic glass: effects of various surface modifications, Mater. Sci. Eng. A 633 (2015) 69–75, https://doi.org/10.1016/j.msea.2015.03.016.
[9] Y. Wang, D. Qu, X. Wang, Y. Cao, X. Liao, M. Kawasaki, S. Ringer, Z. Shan, T. Langdon, J. Shen, Introducing a strain-hardening capability to improve the ductility of bulk metallic glasses via severe plastic deformation, Acta Mater. 60 (2012) 253–260, https://doi.org/10.1016/j.actamat.2011.09.026.
[10] J.F. Li, X. Wang, G.N. Yang, N. Chen, X. Liu, K.F. Yao, Enhanced plasticity of a Fe-based bulk amorphous alloy by thin Ni coating, Mater. Sci. Eng. A 645 (2015) 318–322, https://doi.org/10.1016/j.msea.2015.08.030.
[11] L.W. Ren, Z. Wang, M.M. Meng, H. Tian, H.J. Yang, J.W. Qiao, Plasticity enhancement in bulk metallic glasses by electroless plating with Ni-P amorphous films, J. Non-Cryst. Solids 430 (2015) 115–119, https://doi.org/10.1016/j.jnoncrysol.2015.10.008.
[12] W. Chen, K.C. Chan, P. Yu, G. Wang, Encapsulated Zr-based bulk metallic glass with large plasticity, Mater. Sci. Eng. A 528 (2011) 2988–2994, https://doi.org/10.1016/j.msea.2010.12.077.
[13] M. Meng, Z. Gao, L. Ren, H. Yang, S. Ma, Z. Wang, J. Qiao, Improved plasticity of bulk metallic glasses by electrodeposition, Mater. Sci. Eng. A 615 (2014) 240–246, https://doi.org/10.1016/j.msea.2014.07.033.
[14] B. Chen, S. Pang, P. Han, Y. Li, A.R. Yavari, G. Vaughan, T. Zhang, Improvement in mechanical properties of a Zr-based bulk metallic glass by laser surface treatment, J. Alloys Compd. 504 (2010) S45–S47, https://doi.org/10.1016/j.jallcom.2010.04.053.
[15] G. Wu, R. Li, Z. Liu, B. Chen, Y. Li, Y. Cai, T. Zhang, Induced multiple heterogeneities and related plastic improvement by laser surface treatment in CuZr-based bulk metallic glass, Intermetallics 24 (2012) 50–55, https://doi.org/10.1016/j.intermet.2012.01.022.
[16] G. Wu, R. Li, Z. Liu, B. Chen, T. Zhang, Effects of the laser surface treatment on the mechanical properties of CuZr-based bulk metallic glasses, Sci. China Phys. Mech. Astron. 56 (2013) 925–927, https://doi.org/10.1007/s11433-013-5016-6.
[17] M. Gao, J. Dong, Y. Huan, Y.T. Wang, W.H. Wang, Macroscopic tensile plasticity by scalarizating stress distribution in bulk metallic glass, Sci. Rep. 6 (2016), 21929. https://doi.org/10.1038/srep21929.
[18] Y. Zhang, W.H. Wang, A.L. Greer, Making metallic glasses plastic by control of residual stress, Nat. Mater. 5 (2006) 857–860, https://doi.org/10.1038/nmat1758.

[19] Y. Cao, X. Xie, J. Antonaglia, B. Winiarski, G. Wang, Y.C. Shin, P.J. Withers, K.A. Dahmen, P.K. Liaw, Laser shock peening on Zr-based bulk metallic glass and its effect on plasticity: experiment and modeling, Sci. Rep. 5 (2015), 10789. https://doi.org/10.1038/srep10789.

[20] J. Fu, Y. Zhu, C. Zheng, R. Liu, Z. Ji, Effect of laser shock peening without absorbent coating on the mechanical properties of Zr-based bulk metallic glass, Appl. Surf. Sci. 313 (2014) 692–697, https://doi.org/10.1016/j.apsusc.2014.06.056.

[21] Y. Zhu, J. Fu, C. Zheng, Z. Ji, Structural and mechanical modifications induced on Zr-based bulk metallic glass by laser shock peening, Opt. Laser Technol. 86 (2016) 54–60, https://doi.org/10.1016/j.optlastec.2016.07.003.

[22] Q. Wang, Y. Yang, H. Jiang, C.T. Liu, H.H. Ruan, J. Lu, Superior tensile ductility in bulk metallic glass with gradient amorphous structure, Sci. Rep. 4 (2014), 4757. https://doi.org/10.1038/srep04757.

[23] S.H. Joo, D.H. Pi, A.D.H. Setyawan, H. Kato, M. Janecek, Y.C. Kim, S. Lee, H.S. Kim, Work-hardening induced tensile ductility of bulk metallic glasses via high-pressure torsion, Sci. Rep. 5 (2015), 9660. https://doi.org/10.1038/srep09660.

[24] A. Cherif, Y.S. Pyoun, B. Scholtes, Effects of ultrasonic nanocrystal surface modification (UNSM) on residual stress state and fatigue strength of AISI 304, J. Mater. Eng. Perform. 19 (2009) 282–286, https://doi.org/10.1007/s11665-009-9445-3.

[25] B. Wu, P. Wang, Y.S. Pyoun, J. Zhang, R. ichi Murakami, Study on the fatigue properties of plasma nitriding S45C with a pre-ultrasonic nanocrystal surface modification process, Surf. Coat. Technol. 216 (2013) 191–198, https://doi.org/10.1016/j.surfcoat.2012.11.033.

[26] A. Amanov, I.S. Cho, Y.S. Pyoun, C.S. Lee, I.G. Park, Micro-dimpled surface by ultrasonic nanocrystal surface modification and its tribological effects, Wear 286–287 (2012) 136–144, https://doi.org/10.1016/j.wear.2011.06.001.

[27] C. Ye, A. Telang, A.S. Gill, S. Suslov, Y. Idell, K. Zweiacker, J.M.K. Wiezorek, Z. Zhou, D. Qian, S.R. Mannava, V.K. Vasudevan, Gradient nanostructure and residual stresses induced by Ultrasonic Nano-crystal Surface Modification in 304 austenitic stainless steel for high strength and high ductility, Mater. Sci. Eng. A 613 (2014) 274–288, https://doi.org/10.1016/j.msea.2014.06.114.

[28] J. Liu, S. Suslov, S. Li, H. Qin, Z. Ren, G.L. Doll, H. Cong, Y. Dong, C. Ye, Electrically assisted ultrasonic nanocrystal surface modification of Ti6Al4V alloy, Adv. Eng. Mater. 20 (2018) 1–6, https://doi.org/10.1002/adem.201700470.

[29] H. Zhang, R. Chiang, H. Qin, Z. Ren, X. Hou, D. Lin, G.L. Doll, V.K. Vasudevan, Y. Dong, C. Ye, The effects of ultrasonic nanocrystal surface modification on the fatigue performance of 3D-printed Ti64, Int. J. Fatigue 103 (2017) 136–146, https://doi.org/10.1016/j.ijfatigue.2017.05.019.

[30] J. Liu, S. Suslov, S. Li, H. Qin, Z. Ren, C. Ma, G.X. Wang, G.L. Doll, H. Cong, Y. Dong, C. Ye, Effects of ultrasonic nanocrystal surface modification on the thermal oxidation behavior of Ti6Al4V, Surf. Coat. Technol. 325 (2017) 289–298, https://doi.org/10.1016/j.surfcoat.2017.04.051.

[31] C. Ye, X. Zhou, A. Telang, H. Gao, Z. Ren, H. Qin, S. Suslov, A.S. Gill, S.R. Mannava, D. Qian, G.L. Doll, A. Martini, N. Sahai, V.K. Vasudevan, Surface amorphization of NiTi alloy induced by ultrasonic nanocrystal surface modification for improved mechanical properties, J. Mech. Behav. Biomed. Mater. 53 (2016) 455–462, https://doi.org/10.1016/j.jmbbm.2015.09.005.

[32] C. Ma, H. Qin, Z. Ren, S.C. O'Keeffe, J. Stevick, G.L. Doll, Y. Dong, B. Winiarski, C. Ye, Increasing fracture strength in bulk metallic glasses using ultrasonic nanocrystal surface modification, J. Alloys Compd. 718 (2017) 246–253, https://doi.org/10.1016/j.jallcom.2017.05.056.

[33] C. Ma, G.X. Wang, C. Ye, Y. Dong, Shocking of metallic glass to induce microstructure heterogeneity: a molecular dynamics study, J. Appl. Phys. 122 (2017)https://doi.org/10.1063/1.5000366.

[34] Z.H. Lai, H. Conrad, Y.S. Chao, S.Q. Wang, J. Sun, Effect of electropulsing on the microstructure and properties of iron-based amorphous alloys, Scr. Metall. 23 (1989) 305–310, https://doi.org/10.1016/0036-9748(89)90372-4.

[35] H.Y. Sun, J.S. Wang, L.J. Cao, Q.G. Xue, Effect of electropulsing treatment on the crystallization kinetics of Zr55Ni5Al10Cu30 bulk metallic glass, Thermochim. Acta 537 (2012) 80–85, https://doi.org/10.1016/j.tca.2012.03.011.

[36] H. Mizubayashi, T. Hao, H. Tanimoto, Low temperature crystallization of amorphous alloys under electropulsing, J. Non-Cryst. Solids 312–14 (2002) 581–584, https://doi.org/10.1016/s0022-3093(02)01786-6.

[37] S.B. Qiu, K.F. Yao, Crystallization kinetics of Zr41Ti14Cu12.5Ni10Be22.5 bulk metallic glass in pulsing current pretreatment states, J. Alloys Compd. 475 (2009) 7–10, https://doi.org/10.1016/j.jallcom.2008.07.056.

[38] H. Mizubayashi, T. Takahashi, K. Nakamoto, H. Tanimoto, Nanocrystalline transformation and inverse transformation in metallic glasses induced by electropulsing, Mater. Trans. 48 (2007) 1665–1670, https://doi.org/10.2320/matertrans.MJ200726.

[39] C.Y. Zhang, K.F. Yao, Effects of electropulsing on the glass transition and structural relaxation of a Cu60Zr28Ti12 metallic glass, J. Non-Cryst. Solids 351 (2005) 3663–3666, https://doi.org/10.1016/j.jnoncrysol.2005.09.025.

[40] H. Mizubayashi, S. Okuda, Structural relaxation induced by passing electric current in amorphous Cu50Ti50 at low temperature, Phys. Rev. B 40 (1989) 8057–8060.

[41] P. Yiu, Y.C. Chen, J.P. Chu, S.Y. Chang, H. Bei, J.S.C. Jang, C.H. Hsueh, Rapid relaxation and embrittlement of Zr-based bulk metallic glasses by electropulsing, Intermetallics 34 (2013) 43–48, https://doi.org/10.1016/j.intermet.2012.10.011.

[42] F. Szuecs, C.P. Kim, W.L. Johnson, Mechanical properties of Zr56.2Ti13.8Nb5.0Cu6.9Ni5.6Be12.5 ductile phase reinforced bulk metallic glass composite, Acta Mater. 49 (2001) 1507–1513, https://doi.org/10.1016/S1359-6454(01)00068-4.

[43] H. Choi-Yim, R.D. Conner, F. Szuecs, W.L. Johnson, Processing, microstructure and properties of ductile metal particulate reinforced Zr57Nb5Al10Cu15.4Ni12.6 bulk metallic glass composites, Acta Mater. 50 (2002) 2737–2745, https://doi.org/10.1016/S1359-6454(02)00113-1.

[44] Y. Wu, Y. Xiao, G. Chen, C.T. Liu, Z. Lu, Bulk metallic glass composites with transformation-mediated work-hardening and ductility, Adv. Mater. 22 (2010) 2770–2773, https://doi.org/10.1002/adma.201000482.

[45] G.Y. Wang, P.K. Liaw, A. Peker, M. Freels, W.H. Peter, R.A. Buchanan, C.R. Brooks, Comparison of fatigue behavior of a bulk metallic glass and its composite, Intermetallics 14 (2006) 1091–1097, https://doi.org/10.1016/j.intermet.2006.01.045.

[46] C.L. Qin, W. Zhang, K. Asami, H. Kimura, X.M. Wang, A. Inoue, A novel Cu-based BMG composite with high corrosion resistance and excellent mechanical properties, Acta Mater. 54 (2006) 3713–3719, https://doi.org/10.1016/j.actamat.2006.04.005.

[47] D.C. Hofmann, J.Y. Suh, A. Wiest, G. Duan, M.L. Lind, M.D. Demetriou, W.L. Johnson, Designing metallic glass matrix composites with high toughness and tensile ductility, Nature 451 (2008) 1085–1089, https://doi.org/10.1038/nature06598.

[48] S.F. Guo, L. Liu, N. Li, Y. Li, Fe-based bulk metallic glass matrix composite with large plasticity, Scr. Mater. 62 (2010) 329–332, https://doi.org/10.1016/j.scriptamat.2009.10.024.

[49] Z. Ning, W. Liang, M. Zhang, Z. Li, H. Sun, A. Liu, J. Sun, High tensile plasticity and strength of a CuZr-based bulk metallic glass composite, Mater. Des. 90 (2016) 145–150, https://doi.org/10.1016/j.matdes.2015.10.117.

[50] W. Guo, H. Kato, Development and microstructure optimization of Mg-based metallic glass matrix composites with in situ B2-NiTi dispersoids, Mater. Des. 83 (2015) 238–248, https://doi.org/10.1016/j.matdes.2015.06.033.

[51] P. Yiu, J.S.C. Jang, S.Y. Chang, Y.C. Chen, J.P. Chu, C.H. Hsueh, Plasticity enhancement of Zr-based bulk metallic glasses by direct current electropulsing, J. Alloys Compd. 525 (2012) 68–72, https://doi.org/10.1016/j.jallcom.2012.02.074.

[52] A. Slipenyuk, J. Eckert, Correlation between enthalpy change and free volume reduction during structural relaxation of Zr55Cu30Al10Ni5 metallic glass, Scr. Mater. 50 (2004) 39–44, https://doi.org/10.1016/j.scriptamat.2003.09.038.

[53] A. Van den Beukel, J. Sietsma, The glass transition as a free volume related kinetic phenomenon, Acta Metall. Mater. 38 (1990) 383–389, https://doi.org/10.1016/0956-7151(90)90142-4.

[54] L.L. Wang, L.L. Wang, Z. Nie, Y. Ren, Y. Xue, R. Zhu, H. Zhang, H. Fu, Evolution of residual stress, free volume, and hardness in the laser shock peened Ti-based metallic glass, Mater. Des. 111 (2016) 473–481, https://doi.org/10.1016/j.matdes.2016.09.017.

[55] M.I. Mendelev, M.J. Kramer, R.T. Ott, D.J. Sordelet, D. Yagodin, P. Popel, Development of suitable interatomic potentials for simulation of liquid and amorphous Cu–Zr alloys, Philos. Mag. 89 (2009) 967–987, https://doi.org/10.1080/14786430902832773.

[56] S. Plimpton, Fast parallel algorithms for short-range molecular dynamics, J. Comput. Phys. 117 (1995) 1–19, https://doi.org/10.1006/jcph.1995.1039.

[57] A. Stukowski, Visualization and analysis of atomistic simulation data with OVITO–the Open Visualization Tool, Model. Simul. Mater. Sci. Eng. 18 (2009), 015012. https://doi.org/10.1088/0965-0393/18/1/015012.

[58] S.X. Song, H. Bei, J. Wadsworth, T.G. Nieh, Flow serration in a Zr-based bulk metallic glass in compression at low strain rates, Intermetallics 16 (2008) 813–818, https://doi.org/10.1016/j.intermet.2008.03.007.

[59] S.X. Song, X.L. Wang, T.G. Nieh, Capturing shear band propagation in a Zr-based metallic glass using a high-speed camera, Scr. Mater. 62 (2010) 847–850, https://doi.org/10.1016/j.scriptamat.2010.02.017.

[60] F. Jiang, M.Q. Jiang, H.F. Wang, Y.L. Zhao, L. He, J. Sun, Shear transformation zone volume determining ductile-brittle transition of bulk metallic glasses, Acta Mater. 59 (2011) 2057–2068, https://doi.org/10.1016/j.actamat.2010.12.006.

[61] S.B. Qiu, K.F. Yao, Crystallization behavior of Zr41Ti14Cu12.5Ni10Be22.5 bulk metallic glass under the action of high-density pulsing current, J. Non-Cryst. Solids 354 (2008) 3520–3524, https://doi.org/10.1016/j.jnoncrysol.2008.03.001.

[62] J. Fu, Y. Zhu, C. Zheng, R. Liu, Z. Ji, Effect of laser shock peening on the compressive deformation and plastic behavior of Zr-based bulk metallic glass, Opt. Lasers Eng. 86 (2016) 53–61, https://doi.org/10.1016/j.optlaseng.2016.05.014.

[63] K.R. Lim, J.H. Na, J.M. Park, W.T. Kim, D.H. Kim, Enhancement of plasticity in Ti-based metallic glass matrix composites by controlling characteristic and volume fraction of primary phase, J. Mater. Res. 25 (2010) 2183–2191, https://doi.org/10.1557/jmr.2010.0277.

[64] F. Jiang, Z.B. Zhang, L. He, J. Sun, H. Zhang, Z.F. Zhang, The effect of primary crystallizing phases on mechanical properties of Cu46Zr47Al7bulk metallic glass composites, J. Mater. Res. 21 (2006) 2638–2645, https://doi.org/10.1557/jmr.2006.0315.

[65] C. Zachrisson, H. Kozachkov, S. Roberts, G. Kaltenboeck, R.D. Conner, M.D. Demetriou, W.L. Johnson, D.C. Hofmann, Effect of processing on Charpy impact toughness of metallic glass matrix composites, J. Mater. Res. 26 (2011) 1260–1268, https://doi.org/10.1557/jmr.2011.92.

[66] A. Inoue, W. Zhang, T. Tsurui, A.R. Yavari, A.L. Greer, Unusual room-temperature compressive plasticity in nanocrystal-toughened bulk copper-zirconium glass, Philos. Mag. Lett. 85 (2005) 221–229, https://doi.org/10.1080/09500830500197724.

[67] K. Hajlaoui, B. Doisneau, A.R. Yavari, W.J. Botta, W. Zhang, G. Vaughan, Å. Kvick, A. Inoue, A.L. Greer, Unusual room temperature ductility of glassy copper-zirconium caused by nanoparticle dispersions that grow during shear, Mater. Sci. Eng. A 449–451 (2007) 105–110, https://doi.org/10.1016/j.msea.2006.01.168.

[68] A. Inoue, C. Fan, J. Saida, T. Zhang, High-strength Zr-based bulk amorphous alloys containing nanocrystalline and nanoquasicrystalline particles, Sci. Technol. Adv. Mater. 1 (2000) 73.

[69] T. Egami, Atomic level stresses, Prog. Mater. Sci. 56 (2011) 637–653, https://doi.org/10.1016/j.pmatsci.2011.01.004.

[70] Z. Evenson, T. Koschine, S. Wei, O. Gross, J. Bednarcik, I. Gallino, J.J. Kruzic, K. Rätzke, F. Faupel, R. Busch, The effect of low-temperature structural relaxation on free volume and chemical short-range ordering in a Au49Cu26.9Si16.3Ag5.5Pd2.3 bulk metallic glass, Scr. Mater. 103 (2015) 14–17, https://doi.org/10.1016/j.scriptamat.2015.02.026.

[71] Z. Evenson, R. Busch, Enthalpy recovery and free volume relaxation in a Zr44Ti11Ni10Cu10Be25 bulk metallic glass, J. Alloys Compd. 509 (2011) S38–S41, https://doi.org/10.1016/j.jallcom.2010.12.044.
[72] Z. Evenson, R. Busch, Equilibrium viscosity, enthalpy recovery and free volume relaxation in a Zr44Ti11Ni10Cu10Be25 bulk metallic glass, Acta Mater. 59 (2011) 4404–4415, https://doi.org/10.1016/j.actamat.2011.03.064.
[73] K. Albe, Y. Ritter, D. Şopu, Enhancing the plasticity of metallic glasses: shear band formation, nanocomposites and nanoglasses investigated by molecular dynamics simulations, Mech. Mater. 67 (2013) 94–103, https://doi.org/10.1016/j.mechmat.2013.06.004.
[74] T. Brink, M. Peterlechner, H. Rösner, K. Albe, G. Wilde, Influence of crystalline nanoprecipitates on shear-band propagation in Cu-Zr-based metallic glasses, Phys. Rev. Appl. 5 (2016) 1–16, https://doi.org/10.1103/PhysRevApplied.5.054005.
[75] S. Feng, L. Qi, L. Wang, S. Pan, M. Ma, X. Zhang, G. Li, R. Liu, Atomic structure of shear bands in Cu64Zr36 metallic glasses studied by molecular dynamics simulations, Acta Mater. 95 (2015) 236–243, https://doi.org/10.1016/j.actamat.2015.05.047.
[76] S. Feng, L. Qi, F. Zhao, S. Pan, G. Li, M. Ma, R. Liu, A molecular dynamics analysis of internal friction effects on the plasticity of Zr65Cu35 metallic glass, Mater. Des. 80 (2015) 36–40, https://doi.org/10.1016/j.matdes.2015.05.015.
[77] S.D. Feng, L. Qi, L.M. Wang, P.F. Yu, S.L. Zhang, M.Z. Ma, X.Y. Zhang, Q. Jing, K.L. Ngai, A.L. Greer, G. Li, R.P. Liu, Structural feature of Cu64Zr36metallic glass on nanoscale: densely-packed clusters with loosely-packed surroundings, Scr. Mater. 115 (2016) 57–61, https://doi.org/10.1016/j.scriptamat.2015.12.038.
[78] H.Y. Song, J.J. Xu, Y.G. Zhang, S. Li, D.H. Wang, Y.L. Li, Molecular dynamics study of deformation behavior of crystalline Cu/amorphous Cu50Zr50 nanolaminates, Mater. Des. 127 (2017) 173–182, https://doi.org/10.1016/j.matdes.2017.04.077.
[79] Z. Zhang, J. Eckert, L. Schultz, Difference in compressive and tensile fracture mechanisms of Zr59Cu20Al10Ni8Ti3 bulk metallic glass, Acta Mater. 51 (2003) 1167–1179, https://doi.org/10.1016/S1359-6454(02)00521-9.
[80] P. Lowhaphandu, S.L. Montgomery, J.J. Lewandowski, Effects of superimposed hydrostatic pressure on flow and fracture of a Zr-Ti-Ni-Cu-Be bulk amorphous alloy, Scr. Mater. 41 (1999) 19–24, https://doi.org/10.1016/S1359-6462(99)00128-1.
[81] A.S. Argon, M. Salama, The mechanism of fracture in glassy materials capable of some inelastic deformation, Mater. Sci. Eng. 23 (1976) 219–230, https://doi.org/10.1016/0025-5416(76)90198-1.
[82] F. Spaepen, On the fracture morphology of metallic glasses, Acta Metall. 23 (1975) 615–620, https://doi.org/10.1016/0001-6160(75)90102-9.
[83] L.A. Deibler, J.J. Lewandowski, Model experiments to mimic fracture surface features in metallic glasses, Mater. Sci. Eng. A 527 (2010) 2207–2213, https://doi.org/10.1016/j.msea.2009.10.072.